Modelling the post-cracking behaviour of steel fibre reinforced concrete for structural design purposes

A.G. Kooiman, C. van der Veen and J.C. Walraven
Delft University of Technology, Department of Civil Engineering, Concrete Structures Group

With the increasing number of applications in practice, the demand for standardised test methods and design rules for Steel Fibre Reinforced Concrete (SFRC) arises. Test methods need to be practical, which means that they have to be relatively cheap and simple to carry out. Design models should be easy to use and reliable.
This paper presents a procedure to develop a post-cracking material relation for SFRC by means of inverse analysis. It shows that mean experimental results from three-point bending tests can be simulated with high accuracy using a bilinear stress-crack width relation. After determining the correct procedure to calculate the characteristic values, material safety factors are proposed dependent on the scatter in the post-cracking behaviour. Finally, a material relation is proposed that can be used for structural design purposes.

Key words: **design relation, SFRC, scatter, softening behaviour, reliability**

1. Introduction

Fibre Reinforced Cementitious Composites (FRCC) is the generic term for a large group of composites with a variety of properties. Cementitious composites, such as concrete, are materials that are characterised by brittle failure behaviour in tension. The reason for adding fibres to cementitious composites is to improve this tensile behaviour. Generally speaking, fibres can increase the tensile strength and the ductility of brittle materials. To what extent the tensile behaviour can be improved depends on a number of parameters.
In the past decades a lot of research has been carried out on SFRC. Various efforts have resulted in an increasing number of applications over the past years. Pavements, for example, have been constructed with SFRC in different countries all over the world. Quite recently, SFRC has also been implemented in pilot projects for other applications, such as for the underwater concrete floor at the Potsdamer Platz in Berlin [Falkner & Henke, 1996] and in the prefabricated tunnel segments for a tube section in the Second Heinenoord tunnel, near Rotterdam [Kooiman et al., 1999].
With the increasing number of applications in practice, the demand for standardised test methods and design rules for SFRC arises. Test methods need to be practical, which means they have to be relatively cheap and simple to carry out and design models should be effective, easy to use and reliable. Quite recently, the RILEM Technical Committee 162-TDF published Draft Recommendations on how to test the behaviour of SFRC by means of a standard three-point bending test and how to model the uni-axial behaviour by means of a stress-strain relation [RILEM TC 162-TDF, 2000], as

illustrated by Figure 1. It is the first serious attempt to meet the demand for practical test methods and reliable material relations.

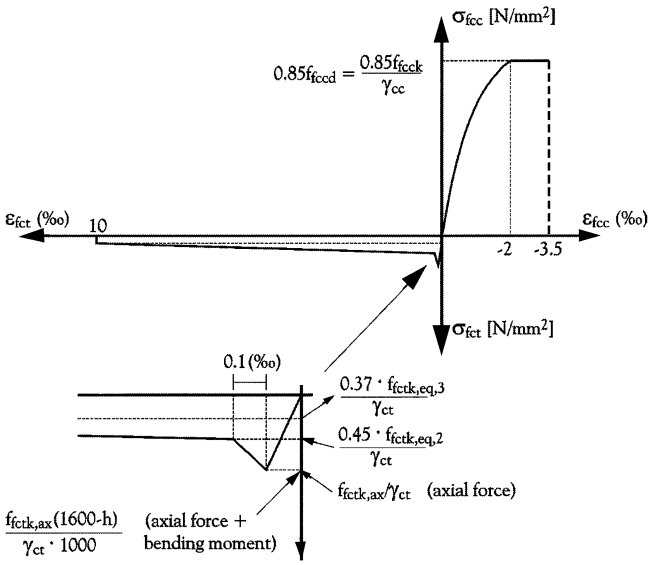

Figure 1: Stress-strain relation for SFRC [RILEM TC 162-TDF, 2000]

Several issues were encountered when modelling the post-cracking behaviour of SFRC according to the stress-strain approach [Kooiman et al., 1997]. One issue was that the derivation of the tensile part of the stress-strain relation, which is illustrated in Figure 1, follows a remarkable procedure. According to this procedure the stress values at specific strain limits in the constitutive material relation are derived from load-deflection diagrams. The curiosity is that these deflections are vertical deformations, measured at mid-span of the beam specimens, and that the procedure relates these deflections of the beam to horizontal strains in the constitutive material relation.
Another important issue encountered was that crack width control, which is important for Serviceability Limit State (SLS) calculations of a SFRC structure, was impossible since the strains could not be translated to discrete deformations.
In addition, test results on standard SFRC beams show that the scatter in the post-cracking behaviour is relatively large compared to the scatter in plain concrete. It was, therefore, unclear whether the material safety factors for plain concrete also apply to the post-cracking behaviour of SFRC.

In this paper, a procedure is proposed to develop a constitutive material relation for the uni-axial post-cracking behaviour of SFRC by means of inverse analysis of load-displacement diagrams, resulting from three-point bending tests on notched SFRC beams. The procedure is developed in such a way that the horizontal deformations in the constitutive material relation can be directly related to the measurements and that the material relation is suitable for crack width control in SLS calculations. Based on experimental research on the scatter in the post-cracking behaviour and standard reliability methods, a design relation is developed for structural design purposes.

Section 2 shows how test results have been obtained and demonstrates that the scatter in the post-cracking behaviour of standard test beams is relatively large when compared to specimens with larger cross-sections. The procedure to compute load-displacement diagrams is explained in Section 3, in which they are compared to mean test results. In Section 4, standard reliability methods have been used to convert the mean material relation into a design relation. It is shown how to calculate characteristic values and how to determine the material safety factor for the post-cracking behaviour of SFRC. Finally, the concluding remarks and future perspectives provide thoughts on the applicability of the design model and future research topics.

2. Experimental research on the post-cracking behaviour of SFRC

2.1 *Research parameters*

The coefficient of variation is a measure for the scatter. As it will be shown in Section 4, the coefficient of variation is an important parameter in the determination of design values in the material model for structural design purposes. Until now, it has never been investigated in what way and to what extent the scatter in the post-cracking behaviour is affected by fibre additions. Before investigating the occurrence of scatter in the post-cracking behaviour of SFRC, it is important to determine the main research parameters. Kooiman [Kooiman, 2000] showed that many parameters influence the post-cracking behaviour of SFRC. It was shown that fibre characteristics, fibre quantity, fibre distribution in the matrix, fibre orientation with regard to the crack plane and the quality of the cementitious matrix surrounding the fibres all affect this behaviour at the same time. Although it is hard to influence fibre orientation and fibre distribution, it is obvious that varying the matrix quality, the fibre characteristics and/or the fibre volume will cause a change in the post-peak behaviour. Table 1 shows the parameters varied in the experimental research carried out within the scope of this research to investigate the occurrence of scatter in the post-cracking behaviour.

Table 1. Main research parameters to investigate scatter in the post-cracking behaviour

Research variables	Parameter	Range
Matrix quality	Compressive strength	59.3 – 81.1 MPa
Fibre volume	Fibre dosage	40 – 60 kg/m^3 (V_f = 0.51-0.77 %)
Fibre characteristics	Aspect ratio L_f/d_f	60 – 80
	Tensile strength fibres	1100 – 2700 N/mm^2

Table 2 shows the mix compositions that have been used in this experimental research in order to provide a difference in matrix quality. In both mixtures glacial river gravel was used with a maximum grain size of 16 mm.

Table 2. Concrete mix compositions used in experiments

Mix components	mix 1	mix 2
Portland cement	87.5 kg/m^3 CEM I 52,5	87.5 kg/m^3 CEM I 52,5
Blast furnace cement	262.5 kg/m^3 CEM III/B 52,5	262.5 kg/m^3 CEM III/B 42,5
Sand 0-4 mm	43 %	48 %
Gravel 4-16 mm	57 %	52 %
Superplasticiser	1.4 % (relative to cement)	1.0 % (relative to cement)
Water/binder ratio	0.42	0.45

Table 3 shows the mean cube compressive strength f_{fccm} and the mean tensile splitting strength $f_{fctm,spl}$ of mix 1 and 2, reinforced with 60 kg/m^3 hooked-end steel wire fibres, having an aspect ratio L_f/d_f of 60/0.75 and a tensile strength of 1200 N/mm^2.

Table 3. Mean compressive and tensile splitting strengths

	f_{fccm} (N/mm^2)	$f_{fctm,spl}$ (N/mm^2)
mix 1	81.1	4.6
mix 2	59.3	3.5

2.2 *Testing method*

In the experimental programme carried out within the scope of this research, the three-point bending test on notched specimens was chosen to investigate the variation in the post-cracking behaviour of SFRC. This choice is based on several arguments.

Firstly, a simple, cheap and reliable test method is necessary to meet the demand from practice for a standard test. The three-point bending test is a reasonably simple, cheap and reliable testing method.

Secondly, structural applications of SFRC (slabs on grade, underwater concrete slabs, shield tunnel linings) mainly concern loading by bending moments. Because of the possibility of redistributing stresses in such statically indeterminate structures, the application of SFRC can increase the load-bearing capacity enormously when compared to the load-bearing capacity of statically determinate members [Schnütgen, 2000]. Before studying the load-bearing capacity of such a structure, the possibility of multiple cracking needs to be examined. However, when testing SFRC mix compositions that are used for slabs and underwater concrete by means of a bending test, only one crack occurs. The location of this single crack cannot be accurately predicted in case of a four-point bending test. A three-point bending test with a notch is much more convenient, because crack initiation is fixed at mid-span.

Thirdly, Kooiman [Kooiman, 1997] showed that in case of SFRC with a relatively high compressive strength and a maximum practical fibre volume, multiple cracking can be observed in a four-point bending test. It was found, however, that the occurrence of more than one crack depended on geometrical boundary conditions, such as the distance between the two point loads on top of the beam. However, before studying crack patterns and crack distances, it is necessary to be able to analyse a single cross-section in bending. The three-point bending test enables the analyses of a single cross-section.
Finally, the three-point bending test has been recommended by a RILEM Committee to test and model the softening behaviour of SFRC [RILEM TC 162-TDF].

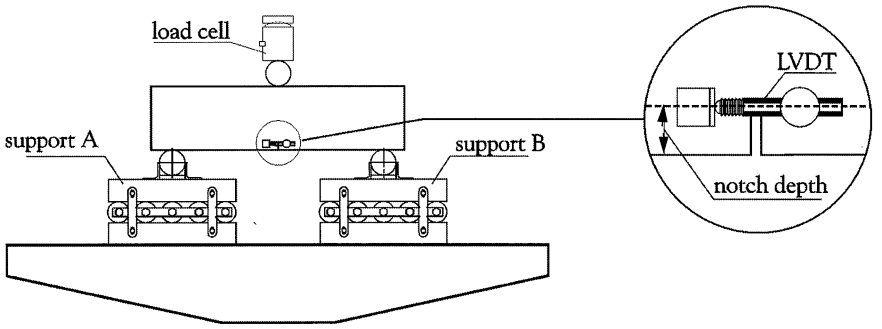

Figure 2: Set-up three-point bending test

Testing frame
The tests were carried out in a stiff, steel test frame. In this frame, the specimens were supported by steel roller supports that were placed on roller support systems (see Figure 2). The central support was connected to a load cell that was fixed to the test frame.

Support systems
For three-point bending tests, Guinea et al. [Guinea et al., 1992] analysed the influence of the experimental equipment on the fracture energy of plain concrete. It was found that energy dissipation at fixed supports resulted in a considerable contribution to the apparent fracture energy, when compared to results with roller bearings. To avoid as much frictional resistance as possible, roller support systems were used to support the beams in the research described below. Two steel rolls with a diameter of 60 mm were fixed on top of the roller support systems. Although in this case both support systems were able to move freely in horizontal direction they slightly differed from each other, as Figure 3 shows. Rubber strips made it possible for one roll to rotate freely so that a restrained deformation as a result of torsion could not occur. Torsion was expected as a result of non-symmetrical size differences and a non-homogeneous fibre distribution in the cross-section.

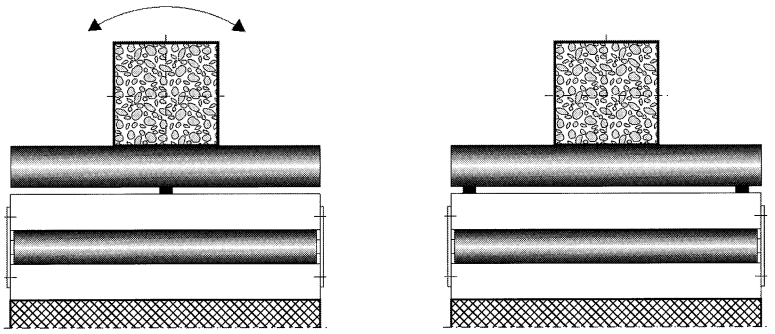

Side view support A Side view support B

Figure 3: Roll support systems

Deformation-controlled testing

To investigate the post-cracking behaviour of steel fibre reinforced concrete it was necessary that the tests were performed on a deformation-controlled basis. This was provided by a closed-loop system, controlled by the deformation measured at the notch tip. Due to the fact that fibres tend to segregate when test specimens are compacted, there is a difference in deformation between both sides. Therefore, it was decided to control the test by averaging the measured deformations on both sides of the specimen. In the initial test series, the deformation rate of testing was 1 mm/s. Later, in the second test series the beams have been loaded up to very large deformations (> 20 mm). The rate of testing in that case was also 1 mm/s. However, after a crack opening displacement of 5 mm had been reached, the rate of testing was increased up to 50 mm/s.

Measurements

To measure the applied loads a load cell was connected to the steel roll on top of the beam that introduced the point load at mid-span. The capacity of this load cell was 400 kN with a measurement accuracy of 0.05 kN. On top of the load cell a hinge was applied to prevent possible effects of restrained deformations due to torsion. Linear variable displacement transducers (LVDT's) were used to measure the crack opening displacement (COD), i.e. the horizontal displacement of the LVDT at the notch tip (see Figure 2), on both sides of the beam. In the initial test series the maximum displacement of these LVDT's was 5 mm with an accuracy of 1.2 μm and the measuring length was 40 mm. In the second test series, the beams were loaded up to larger deformations (> 20 mm) and the maximum displacement of the LVDT's was 100 mm with an accuracy of 21 μm. The measuring length in that case was 100 mm.

2.3 *Test specimens*

The initial test series consisted of six test beams and six cubes of which three cubes have been used to determine the compressive strength and three to check the tensile splitting strength. The rib length of these cubes was 150 mm. These standard compressive and splitting tests were carried out by force-control in a hydraulic press. In case of the tensile splitting tests, 3 mm thick and 15 mm wide strips of triplex were interposed between the loading platens and the specimen. Small test beams (150x150x600 mm^3) were initially poured in steel moulds (size accuracy ± 1.5 mm). These 'standard' beam specimens were compacted by placing the moulds on a vibration table. In addition to the 'standard' beam specimens, larger specimens were also cast (see Figure 4). These specimens were poured in a larger mould with a size accuracy of ± 3.0 mm. They were compacted by means of vibration motors underneath the mould in which they were poured.

According to Bazant [Bazant, 1984], the span length to beam depth ratio l/h has to be higher than $2^1/_2$ to prevent energy dissipation at the supports. Furthermore, the notch depth to beam depth ratio a/h should be in the range of 0.15-0.5 and the notch width should be smaller than half the maximum grain size. The experiments carried out within the scope of this research met the demands of Bazant concerning the dimensions of the test specimens.

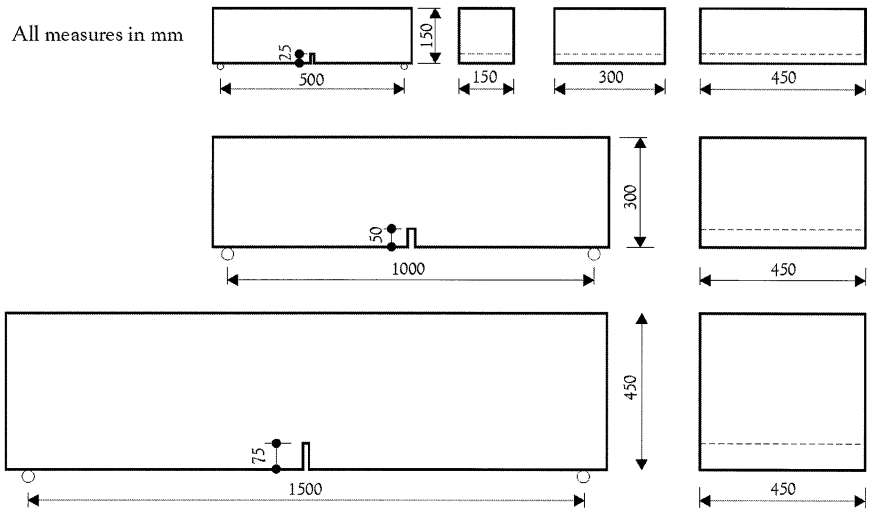

Figure 4: Specimen sizes tested within the scope of this research

In a second test programme, it was decided to pay more attention to the production conditions since these conditions can seriously affect the test results. The latter will be shown in the next section. The procedure for casting the specimens and filling the moulds is shown in Figure 5a, according to the Draft Recommendation of the RILEM TC 162 TDF [RILEM TC 162-TDF, 2000]. All specimen sizes were cast in one large mould so that the vibration conditions were similar for all specimen sizes. After the specimens were compacted, plastic cover sheets were used to prevent early drying of the specimens. All specimens were stored in the laboratory for 1 or 2 days (at a temperature varying from 18 to 24 degrees Celcius) until they could be demoulded and placed into a climate-conditioned

room at a constant temperature of 20 degrees Celcius and a relative humidity of approximately 99%. All test specimens were tested at an age of 28 days ± 1 day. The loading direction was perpendicular to the pouring direction (see Figure 5b). Before testing, the specimens were notched with the help of a diamond saw.

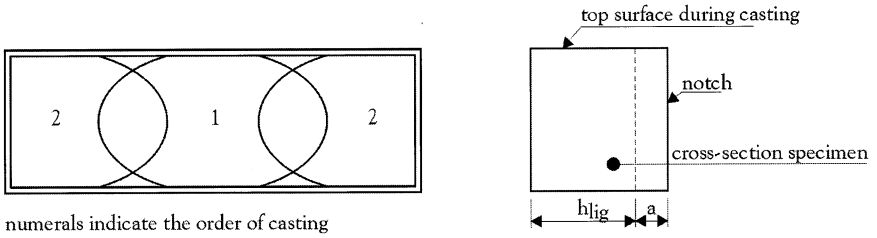

(a) Filling order *(b) Filling direction*

Figure 5: Filling procedure for casting the specimen [RILEM TC 162-TDF, 2000]

2.4 *Test results*

Determination of energy absorption capacity G_{fc} *and coefficient of variation* V_G

To analyse the post-cracking behaviour of SFRC, it is common practice to determine toughness values. The toughness of steel fibre reinforced concrete D_{fc} is determined by calculating the area under the load-displacement curve [ACI Committee 544, 1988]. In case of SFRC, the ductility increases considerably compared to plain concrete. Therefore the tail of the load-displacement diagram is often cut at displacements that are 10 to 20 times larger than the maximum displacement for plain concrete, [RILEM TC 162-TDF, 2000]. Usually the surface below the linear elastic part of the load-displacement diagram is subtracted from the total toughness value of SFRC to determine the effect of the fibre addition. In case of low fibre volumes, this is necessary to determine the real contribution of the fibre addition. In case of the fibre volumes applied within the scope of this research, however, the surface beneath the linear elastic branch of the load-displacement diagrams is negligible compared to the considered toughness values of SFRC. Therefore, the contribution of the concrete matrix has been taken into account in the toughness values presented hereafter.

According to RILEM TC-89 FMT [RILEM TC-89 FMT, 1990], the energy absorption capacity G_{fc} of the cross-section can be calculated by dividing the toughness D_{fc} by the beam's cross-section. With the beam width b, beam depth h and notch depth a, this becomes:

$$G_{fc}(\delta) = \frac{D_{fc}(\delta)}{b \cdot (h - a)} \tag{1}$$

In the determination of the total toughness D_{fc}, the effect of the specimen's weight is accounted for by the additional toughness $\Delta D_{fc,w}$, illustrated by the shaded area in Figure 6. In this case, the tests were stopped at a deformation δ_s. To account for the weight-effect, in this chapter only the contribution $\Delta D_{fc,w}$ up to the deformation at test stop is taken into account (see Figure 6). The triangle OO'O'' is not accounted for, as its contribution to D_{fc} is negligible. $\Delta D_{fc,w}$ as displayed in Figure 6, however,

is considerably exaggerated for reasons of illustration. Calculations showed that in case of the SFRC mixtures under consideration, the contribution to the energy absorption capacity of the triangle OO'O'' was less than 1% at δ_s = 2.0 mm. In addition, the dead load that was accounted for in these calculations was less than 1% of the maximum load.

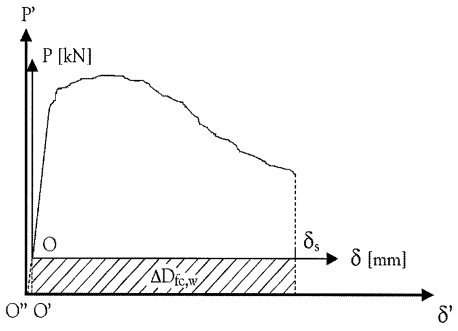

Figure 6: Contribution to the total toughness of the specimen's weight

With $G^i_{fc}(\delta)$ as the energy absorption capacity of the i^{th} test specimen at crack opening displacement δ and $G_{fcm}(\delta)$ as the mean value of the energy absorption capacity of the test series (consisting of n tests), the standard deviation $s_G(\delta)$ was calculated as follows:

$$s_G(\delta) = \sqrt{\frac{\sum_{i=1}^{n}(G^i_{fc}(\delta) - G_{fcm}(\delta))^2}{n-1}} \qquad (2)$$

The scatter in the post-cracking behaviour of SFRC can be quite large, which causes a high standard deviation. At the same time the mean value of the energy absorption capacity can vary significantly. To visualise the combined effect, the coefficient of variation V_G can be determined by the following equation:

$$V_{G(\delta)} = \frac{s_{G(\delta)}}{G_{fcm(\delta)}} \qquad (3)$$

Effect of matrix quality on mean G_{fc} values and coefficient of variation V_G

Characteristic load-displacement (P-δ) curves as a result of bending tests on 'standard' SFRC specimens (150×150×600 mm^3) are shown in Figures 7 and 8 for mix 1 and 2 of Table 2. To both mixtures 0.77 % (or 60 kg/m^3) of hooked-end (low carbon) steel wire fibres were added with an aspect ratio of 80 (L_f/d_f = 60/0.75). As Figures 7 and 8 show, a considerable scatter occurred in the post-cracking stage of the test results. It is obvious that the scatter in the higher strength SFRC of mix 1 exceeds the scatter in the test results of mix 2.

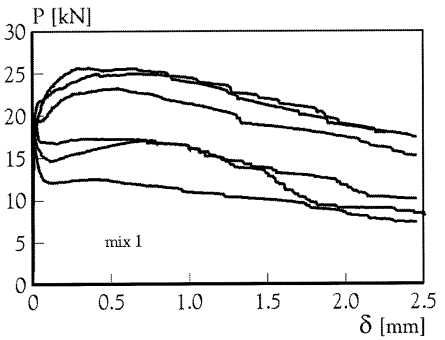

Figure 7: Load-displacement curves mix 1
(f_{fccm} = 81.1 N/mm², V_f = 0.77%, L_f/d_f = 60/0.75)

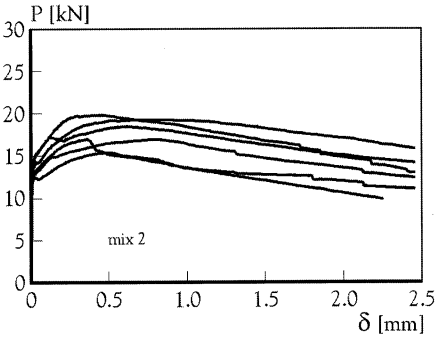

Figure 8: Load-displacement curves mix 2
(f_{fccm} = 59.3 N/mm², V_f = 0.77%, L_f/d_f = 60/0.75)

Figure 9 shows the effect of the concrete strength on the mean energy absorption capacity G_{fcm}. The mean G_{fc} values for crack openings up to 2.5 mm are lower for the lower strength concrete. It can be seen that within the tested range of deformation, the energy absorption capacity G_{fcm} of the cross-section increases almost linearly. Figure 10 shows that the coefficient of variation V_G, which is a function of the displacement, is considerably smaller for the lower strength SFRC of mix 2. Initially, it was thought that this was due to the fact that the fibres tended to break in the high strength matrix of mix 1, which was clearly heard during execution of the tests. Hereafter, however, it will be shown that fibre rupture has nothing to do with the steep increase in V_G just after first cracking.

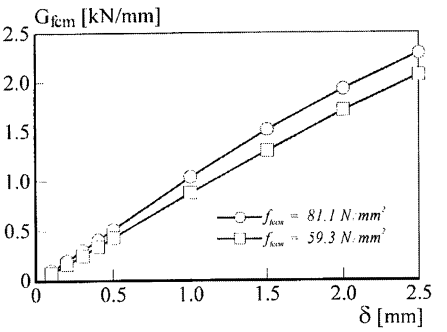

Figure 9: Effect of concrete strength on G_{fcm}
(low carbon fibres: V_f = 0.77%, L_f/d_f = 60/0.75)

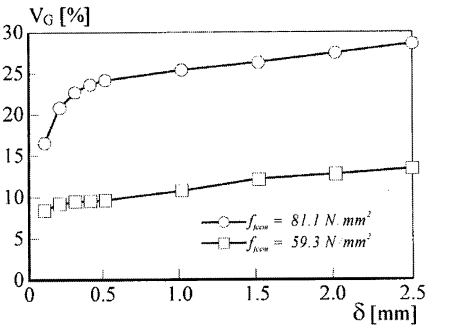

Figure 10: Effect of concrete strength on V_G
(low carbon fibres: V_f = 0.77%, L_f/d_f = 60/0.75)

Effect of fibre characteristics on mean G_{fc} values and coefficient of variation V_G

To investigate the effect of fibre rupture on the magnitude of scatter in the post-cracking behaviour, the high strength concrete matrix of mix 1 has also been tested with two other fibre additions. The first was 0.77% of hooked-end high carbon steel wire fibres with a tensile strength of 2700 N/mm^2 (and L_f/d_f = 60/0.75) and the second was 0.77% of hooked-end low carbon steel wire fibres with a tensile strength of 1100 N/mm^2 (and L_f/d_f = 60/0.92). These fibre additions were chosen such that fibre rupture was prevented.

Figure 11 shows that the mean G_{fc} values were not very sensitive to the change in aspect ratio (from 80 to 65) and to an increase in fibre strength (1100 N/mm^2 for low carbon fibres and 2700 N/mm^2 for high carbon fibres). Figure 12 shows that the aspect ratio and the fibre strength do not really affect the coefficient of variation V_G in this particular range of deformations. It seems as if the fibre type does not influence the post-cracking behaviour as much as the concrete strength.

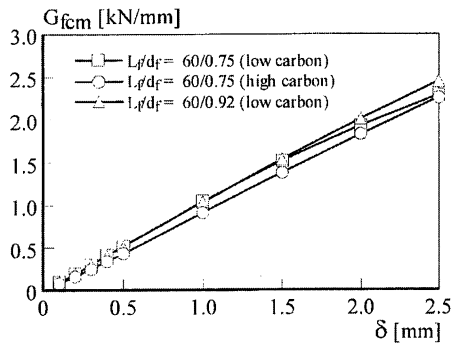

Figure 11: Effect of fibre characteristics on G_{fcm} (mix 1: f_{fccm} = 81.1 N/mm^2; V_f = 0.77%)

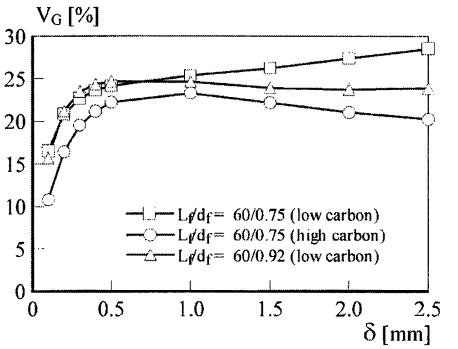

Figure 12: Effect of fibre characteristics on V_G (mix 1: f_{fccm} = 81.1 N/mm^2; V_f = 0.77%)

In a second experimental programme various bending tests have been carried out up to very large deformations. In this case mix 2 was used instead of mix 1. Not only a 60 kg/m^3 fibre addition was tested with an aspect ratio of 60/0.75 = 80, but also a mixture with fibres having an aspect ratio of 30/0.5 = 60. The mean values of the energy absorption capacity have been plotted in Figure 13. It is obvious that the aspect ratio significantly influences the mean energy absorption capacity at larger deformations than 2.5 mm. On the other hand, Figure 14 confirms that the effect of the aspect ratio on the coefficient of variation V_G is relatively small.

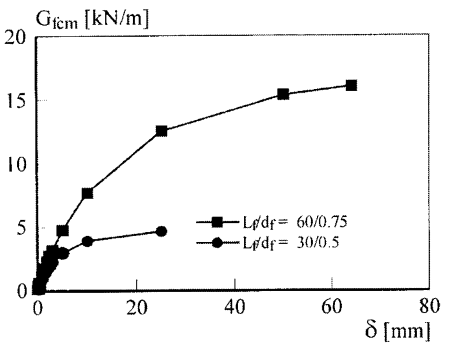

Figure 13: Effect of aspect ratio on G_{fcm} (mix 2: f_{fccm} = 59.3 N/mm², V_f = 0.77%)

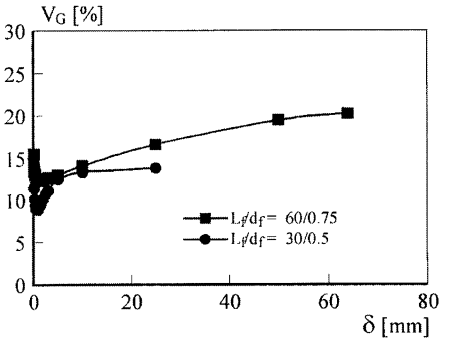

Figure 14: Effect of aspect ratio on V_G (mix 2: f_{fccm} = 59.3 N/mm², V_f = 0.77%)

Effect of fibre volume on mean G_{fc} values and coefficient of variation V_G

To investigate the effect of fibre volume on the occurrence of scatter in the post-cracking behaviour two different fibre volumes have been added to mix 2. Figure 15, as expected, shows that the mean G_{fc} values decreased as the added fibre volume was decreased. At the same time Figure 16 shows that the coefficient of variation is much higher for the mix with the lower fibre volume. It is obvious that the scatter in the post-cracking behaviour increases considerably as the added fibre quantity is lowered. Again the steep increase occurs just after cracking, within the first 0.5 mm of deformation.

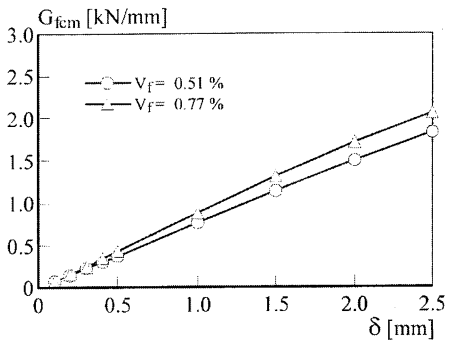

Figure 15: Effect of fibre characteristics on G_{fcm} (mix 2: f_{fccm} = 59.3 N/mm², L_f/d_f = 60/0.75)

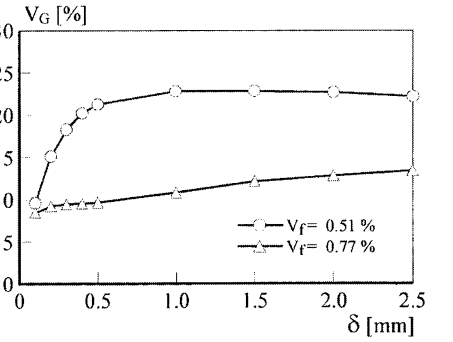

Figure 16: Effect of fibre characteristics on V_G (mix 2: f_{fccm} = 59.3 N/mm², V_f = 0.77%)

Effect of an increasing beam width on the mean G_{fc} values and scatter

To determine the effect of the beam width b, mean G_{fc}-values at a crack opening displacement of 2.0 mm ($G_{fcm,2.0}$) have been compared for different beam widths. Figure 17a shows the $G_{fcm,2.0}$-values of

specimens manufactured with mix 1 for three beam widths. In Figure 17b, $G_{fcm,2.0}$ is presented for mix 2.

Quite surprisingly, the value of $G_{fcm,2.0}$ increased with an increasing beam width b, although the increase is relatively small after b = 300 mm. $G_{fcm,2.0}$ was expected to be independent of the beam width, according to equation (1). If any influence could be expected, this would be a decrease in $G_{fcm,2.0}$ with b, because of a smaller boundary effect. This large deviation can only be caused by differences in the filling and compacting procedure between the 'standard' beams (b = 150 mm) and the wider test specimens, since all other conditions (mix composition, fibre addition, dimensions) were held constant.

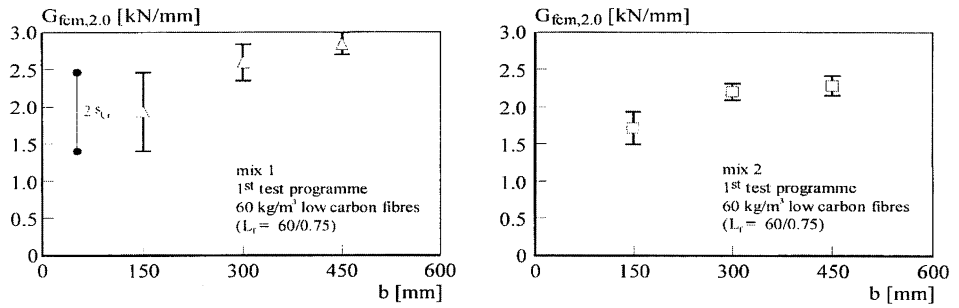

(a) mix 1: f_{fccm} = *81.1 N/mm²;* V_f = *0.77%*

(b) mix 2: f_{fccm} = *59.3 N/mm²,* V_f = *0.77%*

Figure 17: Effect of beam width on energy absorption capacity $G_{fcm;2.0}$ *and standard deviation* s_G

As it was mentioned earlier, in a second test programme the production techniques used to manufacture the test specimens were kept as similar as possible for all specimen sizes. After repeating the test series on mix 2, Figure 18 shows that the energy absorption capacity $G_{fcm,2.0}$ is more or less constant. The $G_{fcm;2.0}$-values do not deviate much from one another and are comparable to the $G_{fcm,2.0}$-values shown in Figure 17b, except for the 'standard' test specimens with b = 150 mm.

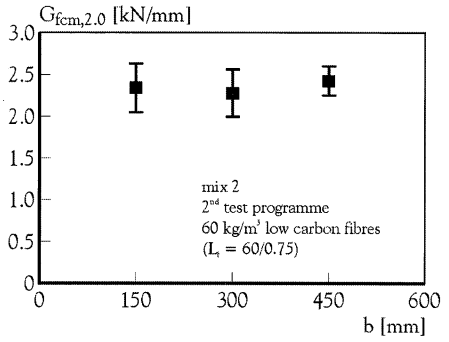

Figure 18: Effect of increasing beam width on $G_{fcm,2.0}$

To investigate this phenomenon, the number of fibres in the cross-sections was counted after breaking the test specimens and dividing the crack faces into five layers of each 25 mm deep (see Figure 19).

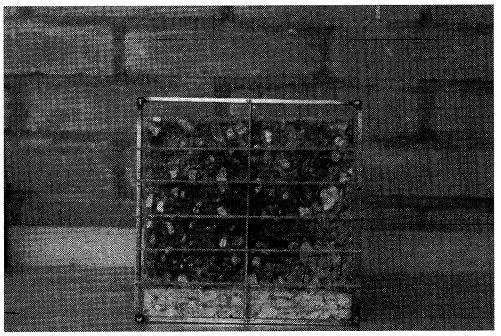

Figure 19: Determination of the number of fibres in a cross-section

In Figure 20 and 21 the number of fibres per cross-sectional area is plotted for mix 2 and increasing beam widths. Figure 20 presents the mean number of fibres per cm^2 in the beams of the initial test series of which the $G_{fcm,2.0}$ values were shown in Figure 17b. Figure 21 represents the mean number of fibres in the beams of the second test series of which the $G_{fcm,2.0}$ values are shown in Figure 18.

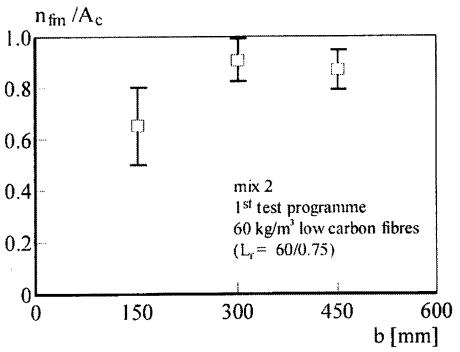

Figure 20: Number of fibres per cm^2 in 1st test series

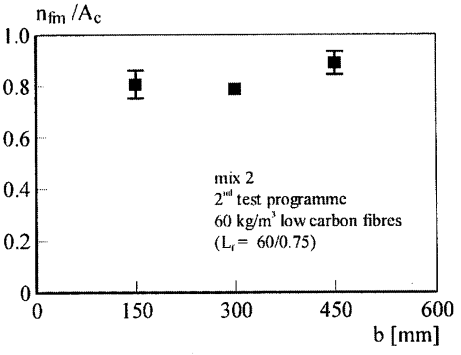

Figure 21: Number of fibres per cm^2 in 2nd test series

Figure 20 shows that the number of fibres per cm^2 is lower in the 150 mm wide beams than in the wider beams. This is rather strange since the added fibre quantity was not altered. On the other hand, Figure 21 shows that the number of fibres per cross-sectional area was more or less constant in case of the additional test series, in which all beams were poured and compacted in the same way. In the first test series, the filling mode of the moulds and the compacting process of the small beams caused a smaller number of fibres at mid-span.

When comparing Figure 20 to Figure 17b and Figure 21 to Figure 18 it looks like the energy absorption capacity is related to the number of fibres in the crack plane. This confirms the findings of

Stroband [Stroband, 1998] who found a strong correlation between the number of fibres in the cross-section and the fracture energy derived from uni-axial tensile tests.

Effect of the beam depth on the mean G_{fc} values and scatter

Figure 22 shows the effect of the beam depth h on the mean energy absorption capacity G_{fcm} and the standard deviation s_G at a crack opening of 2.0 mm. The presented figure results from the test series on 450 mm wide beams made of mix 1 of Table 2. It looks like there is no size-effect, since the mean values do not deviate much from each other (< 10%). Furthermore, it seems that the beam depth does not influence the scatter. Figure 23 shows that the coefficient of variation is quite small (5%) in this range of deformation.

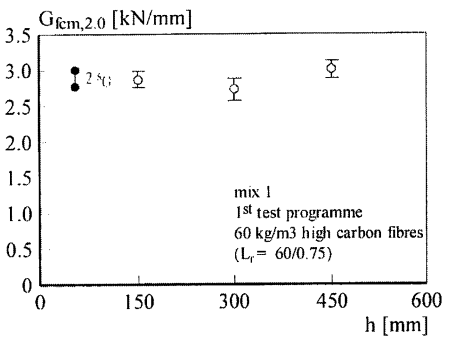

Figure 22: Effect of beam depth on $G_{fcm,2.0}$

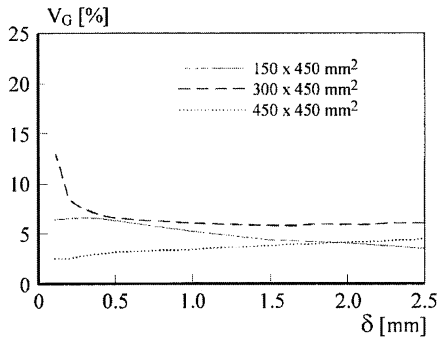

Figure 23: Effect of beam depth on V_G

2.5 *Discussion of test results*

The test results showed that the concrete strength, the fibre volume and the specimen size are the most dominating parameters that cause scatter in the post-cracking behaviour of SFRC.

After increasing the concrete quality (from f_{fccm} = 59.3 N/mm^2 of mix 2 to f_{fccm} = 81.1 N/mm^2 of mix 1), the coefficient of variation increased considerably. The combination of concrete quality and fibre volume seemed very critical. The matrix strength was increased to such a level that at crack initiation the mean pull-out load per fibre in the section of the beam just above the notch approached the maximum pull-out load of the fibre type. In the case that there were few fibres located near the mostly stressed zone, the fibres immediately broke/slipped and the load-displacement curve dropped after crack initiation (see the three 'dropping' curves in Figure 7). On the other hand, in the cases that many fibres were located in the most stressed zone, the applied load in the bending test increased after crack initiation. This can be explained by the fact that the mean pull-out load per fibre is lower than the maximum pull-out load. Obviously, the fibre distribution starts to play an important role at the considered critical combination of concrete strength (f_{fccm} = 81.1 N/mm^2) and fibre volume (V_f = 0.77%).

By decreasing the fibre volume in mix 2 (from $V_f = 0.77\%$ to $V_f = 0.5\%$), it was confirmed that the scatter increased as the number of fibres decreased. The considered combination of concrete strength ($f_{fccm} = 59.3$ N/mm^2) and fibre volume ($V_f = 0.5\%$) resulted in a similar magnitude of the coefficient of variation as in case of the critical combination of mix 1 ($f_{fccm} = 81.1$ N/mm^2) and 60 kg/m^3 ($V_f = 0.77\%$) of hooked-end steel wire fibres.
Although material size effects in the post-cracking behaviour of SFRC were not observed, some size-related effects were found that seem to be of significance when modelling the post-cracking behaviour of SFRC. The size of the cross-section, for instance, strongly affects the scatter in the post-cracking behaviour. It was observed that in case of critical combinations of matrix quality and fibre volume, the scatter decreased considerably when the size of the loaded cross-section was increased.

3. Modelling the post-cracking behaviour of SFRC

3.1 *Computational procedure*

As Section 2 showed, the three-point bending test was chosen to test the post-cracking behaviour of SFRC. The tests, however, do not immediately result in a stress-crack opening relation that is suitable for the use in design calculations.

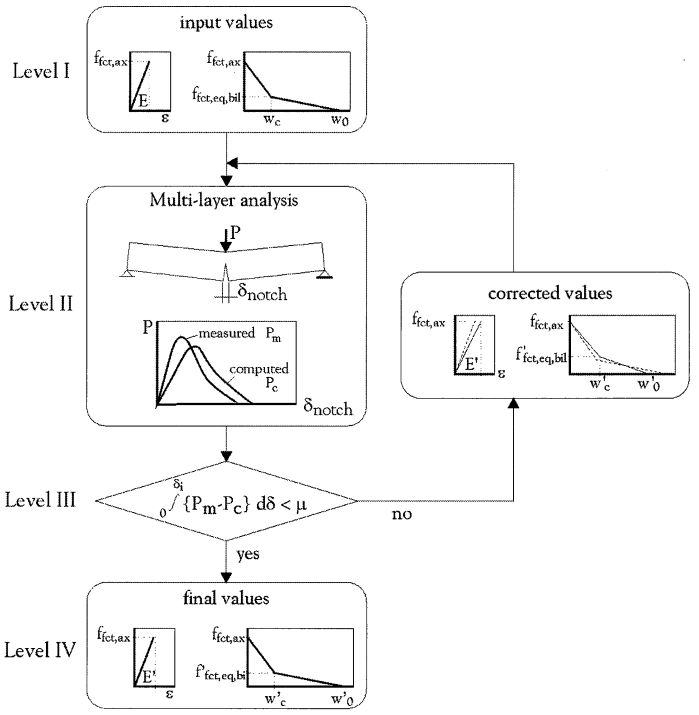

Figure 24: Inverse modelling procedure [Roelfstra & Wittman, 1986]

Figure 24 shows a schematic representation of the inverse modelling procedure according to Roelfstra and Wittmann [Roelfstra & Wittman, 1986]. It can be subdivided into four levels. The first level is the input level. On this level geometrical boundary conditions are set and assumptions are made concerning the uni-axial behaviour of the composite material. The second level is the numerical level where the fracture geometry under consideration is analysed, which in this case is the cross-section of a notched SFRC beam. The third level is the level where the accuracy of the load-crack opening displacement is checked. On this level, the deviation between the computational and experimental results is calculated. Depending on this deviation and the permissible error, the analysis is repeated using a modified softening diagram until the error is smaller than the predefined accuracy. The fourth level is the output level, presenting the final parameters of the tensile softening diagram.

Level I: the input level

In the input level of the inverse modelling approach, geometrical boundary conditions and the uni-axial material behaviour are set. In this modelling procedure, the effective beam depth h_{lig} (beam depth minus notch depth), the beam width b and the span length l are input parameters concerning the geometry of the specimen. In addition, the uni-axial material behaviour of SFRC is defined by setting three material relations:

1. A stress-strain diagram for SFRC in compression (see Figure 25a). In the analyses of SFRC cross-sections, the compressive behaviour is described by the mean compressive strength and an assumption concerning the linear elastic and ultimate strain limits. The linear elastic strain limit in compression is set at 1.75‰, which corresponds to the design codes for structural concrete. Kooiman [Kooiman, 2000] showed that the influence of the initially assumed post-peak behaviour in compression can be relatively large. It was shown that assuming a linear post-peak behaviour up to an ultimate strain limit of 10‰ leads to good results.
2. A stress-strain diagram for SFRC in linear elastic tension. The linear elastic behaviour in tension is determined by the uni-axial tensile strength of the SFRC under consideration and the linear elastic strain limit. The uni-axial tensile strength $f_{fctm,ax}$ is related to the tensile splitting strength $f_{fctm,spl}$ of the mix composition under consideration. Körmeling [Körmeling, 1986] showed that in the case of SFRC test specimens made of similar mix compositions as were used in the scope of this research, the axial tensile strength to splitting strength ratio was in the range of 0.7-0.8. The linear elastic strain limit is chosen in such a way that the linear elastic branch of the computed P-d curves fits the elastic part of the measured curves.
3. A stress-crack width relation for the post-cracking behaviour of SFRC. As the next Section will show, a bilinear softening relation for SFRC can satisfy both demands, depending on the parameters in this relation (see Figure 25b) and the other input parameters in the inverse modelling procedure. For physical reasons, the input value of w_0 cannot exceed the maximum embedded fibre length of $^1/_2 L_f$. Kooiman [Kooiman, 2000] showed that the crack width w_0 can be related to the average projected embedded fibre length. The only parameters to be varied in the inverse modelling procedure are the equivalent post-cracking strength $f_{fctm,eq,bil}$ and the characteristic crack width w_c.

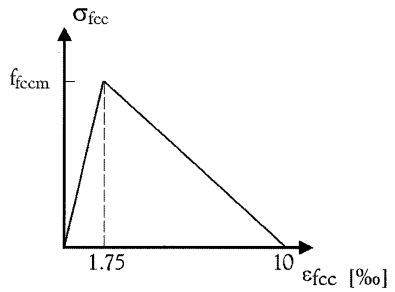

(a) Input relation for SFRC in compression

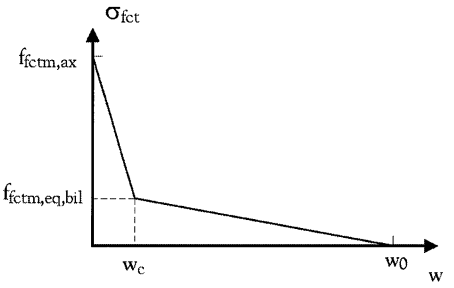

(b) Input relation for the post-cracking behaviour of SFRC

Figure 25: Material relations for SFRC

Level II: the simulation level

The simulation procedure used in level II of the inverse modelling procedure is based on the so-called multi-layer procedure developed by Hordijk [Hordijk, 1991]. This simulation procedure was used by Hordijk to study the bending behaviour of plain concrete. The reason for analysing SFRC cross-sections by means of the multi-layer procedure is because of the simplicity of the model. It can be easily programmed in a spreadsheet, in which parameters can be easily varied to investigate the effect of each parameter.

In contrast to Hordijk, who simulated load-deflection curves for plain concrete, the multi-layer procedure was used in the scope of this research to simulate and analyse load-crack opening displacement diagrams, such as those resulting from three-point bending tests as described in Section 2.

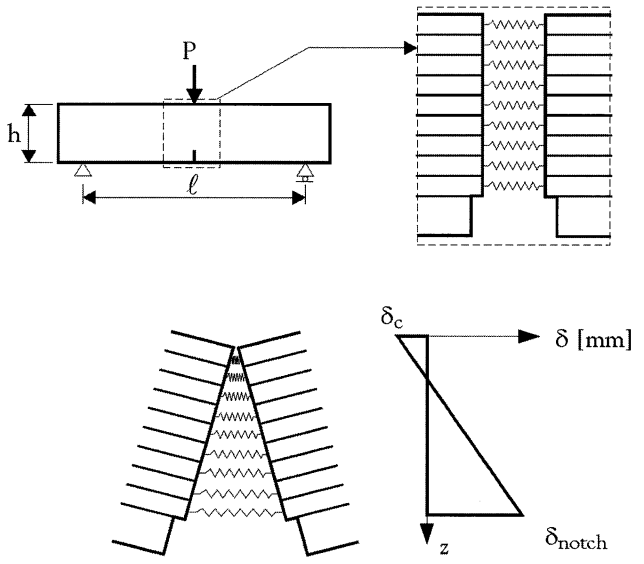

Figure 26: First basic principle of the multi-layer simulation procedure [Hordijk, 1991]

The multi-layer procedure is based on three principles. Figure 26 demonstrates the first principle of the multi-layer procedure. It shows that the beam is divided into two halves, which are connected by springs above the notch. Each spring represents the behaviour of a small layer. Furthermore, it is assumed that a linear displacement distribution describes the deformation over the effective beam depth.
The second principle of the procedure is demonstrated in Figure 27. For each spring the deformation is determined by calculating the average deformation in the corresponding layer. For each layer, the stress can be determined from the stress-displacement relation of the springs. From the linear deformation distribution the corresponding contributions to the normal force N and the bending moment M are calculated for each layer. After adding the contributions of all layers, the internal force N and bending moment M are known. Equilibrium is found when N is equal to zero. The corresponding internal bending moment is equal to the external bending moment caused by the applied load on the beam. As a result, the external load can be easily determined from the internal bending moment.

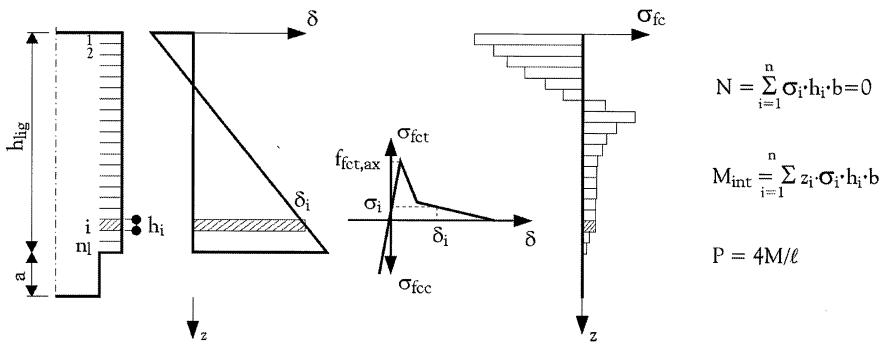

Figure 27: Second basic principle of the multi-layer simulation procedure [Hordijk, 1991]

The third principle of the model is the incremental procedure. In small steps the displacement at the notch tip is increased with a marginal displacement $\Delta\delta_{notch}$. After each step, iteration is necessary to accomplish the equilibrium of forces in the cross-section: the displacement at the top of the beam d_c is adjusted until N is equal to zero. At this state of equilibrium, the crack opening displacement at the notch tip δ_{notch} and the bending load P that corresponds to the bending moment M, are plotted. By repeating the incremental steps, the load-crack opening displacement diagram is simulated, as Figure 28 demonstrates.

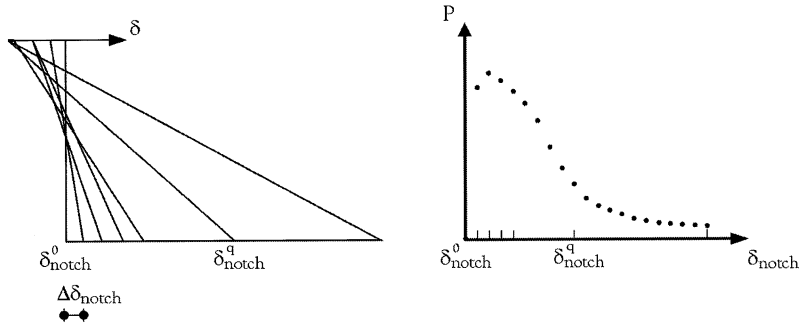

Figure 28: Third basic principle of the multi-layer simulation procedure

The multi-layer simulation seems quite straightforward to carry out. However, the stress-displacement characteristic of the springs is a combination of the uni-axial material relations set in the input level: the stress-strain relation for the compressive zone, the linear elastic tensile relation for the uncracked tensile zone and the stress-crack width relation for the cracked tensile zone. To combine these relations and produce a linear deformation distribution over the beam depth (as shown in Figure 28), Hordijk introduced the influence length l_i. By multiplying this parameter with relative deformations in compression and in linear elastic tension, strains are converted to discrete displacements so that load-crack opening displacement diagrams can be computed and compared to the mean results of three-point bending tests.

In his multi-layer simulations, Hordijk [Hordijk, 1991] showed that the influence length l_i strongly affects the maximum load-bearing capacity of plain concrete cross-sections in bending and hardly influences the tail of the load-deflection curves. To check whether or not the same effects apply on the load-crack opening displacement diagrams, the exercise done by Hordijk was repeated. Figure 29 shows the input relations that describe the uni-axial behaviour of the concrete under consideration.

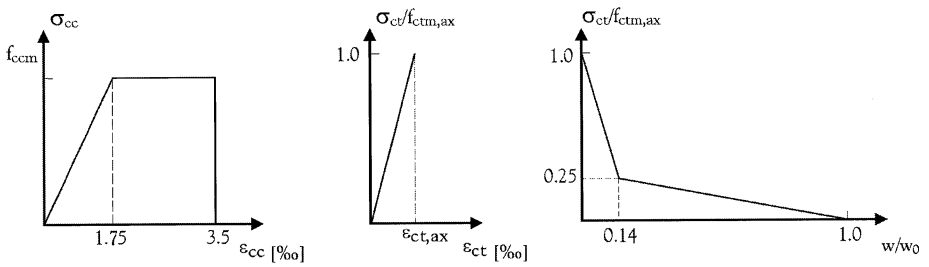

(a) σ–ε relation for compression *(b) Linear elastic tensile behaviour* *(c) Tensile softening behaviour*

Figure 29: Input relations for plain concrete

For concrete in compression, Figure 29a illustrates the bilinear stress-strain relation according to the Dutch design regulations for concrete structures. The simulations are carried out for mix 2 of Table 2, without the addition of fibres. As the concrete compressive strength is not influenced by the addition of fibres, the mean cube compressive strength is assumed to be equal to 59.3 N/mm^2. The linear elastic behaviour in tension is often defined by the uni-axial tensile strength $f_{fct,ax}$ and the corresponding strain limit $\varepsilon_{ct,ax}$ (see Figure 29b). According to tensile tests carried out by Körmeling [Körmeling, 1986] on plain concrete with a mean cube compressive strength f_{ccm} of 55-60 N/mm^2, the displacement at the peak load was equal to 0.02 mm. The measuring length applied by Körmeling was 100 mm. Hence, the strain limit was equal to 0.2 ‰. The mean uni-axial tensile strength $f_{ctm,ax}$ in case of the tests of Körmeling was equal to 2.8 N/mm^2 for a testing rate of 0.125 μm per second. Figure 29c illustrates the assumed bilinear tensile softening relation for plain concrete, as proposed by Wittmann et al. [Wittmann et al., 1988]. In this case, the crack width w_0 was set at 0.5 mm.

Using the input material relations of Figure 29 in the multi-layer procedure, Figure 30 shows the effect of the influence length l_i in case of 'standard' beam specimens (see Section 2.3). Obviously, the influence length has the same impact on the load-crack opening displacement diagrams as Hordijk's fictitious length on the load-deflection diagrams. Figure 30a shows that the peak load decreases when the influence length increases and that the tail of the bending behaviour is not affected. It can also be observed that the effect of the influence length on the pre-peak behaviour is relatively large. This is no surprise since the concrete stiffness in the procedure is directly related to the influence length ($\delta_c = \varepsilon_{fcc} \cdot l_i$).
In SFRC for practical applications, the uni-axial compressive and tensile strength is not really affected by adding steel fibres to the mix. When it is assumed that these strength values remain the same as in Figure 30a, Figure 30b shows that the effect of the influence length on the flexural behaviour of SFRC is much smaller than in case of plain concrete. Figure 30b is the result of multi-layer simulations in which the post-peak behaviour is adjusted according to the assumptions considering the material relations, as was mentioned before.
Although the maximum load-bearing capacity of SFRC is not very sensitive to the exact value of the influence length l_i, the effect of l_i on the rotational capacity of the cross-section is relatively large. The exact definition of the influence length is, therefore, quite a relevant issue. Pederson [Pederson, 1996], compared similar calculations with finite element calculations and found that $l_i = 0.5 \cdot h_{lig}$ is suitable.

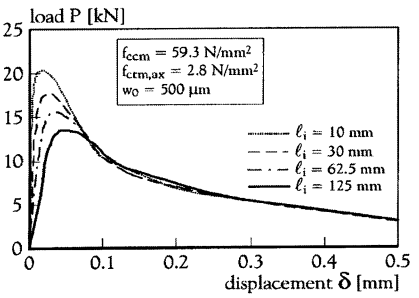

(a) Effect of l_i in case of plain concrete

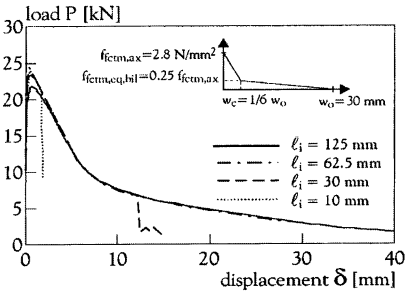

(b) Effect of l_i in case of SFRC

Figure 30: Effect of the influence length l_i on simulated P-δ curves

In addition to the influence length, the number of layers n applied in the multi-layer model also affects the computed P-δ curves. Figure 31 shows the effect of the applied number of layers n_l. Obviously, the number of layers influences the peak load. Just like in Finite Element calculations, a balance needs to be found between the accuracy of simulations and the computational time that is necessary to carry out the analysis. In the scope of this research, this balance was found at n_l = 500. An increase in the number of layers hardly affects the P-δ curve, but strongly increases the computational time.

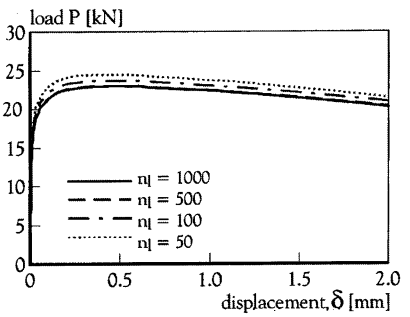

Figure 31: Effect of the number of layers in the multi-layer simulations

Level III: the accuracy check

In the inverse modelling procedure carried out in this paper, two checks are programmed to determine the accuracy of the simulations. Firstly, the area under the simulated P-δ curve is compared to the area under the measured P-δ curve. The simulated results are rejected when the maximum devi-

ation in toughness $\Delta D_{fc,max}$ of 10% is exceeded (see Figure 32). In reality, the displacements do not reach a final value. For that reason, the tail is cut at a displacement where the tail of the P-δ curve is almost horizontal. In case of 30 mm long fibres, the tail was cut at a displacement of 20 mm, whereas for 60 mm long fibres this displacement was 70 mm.

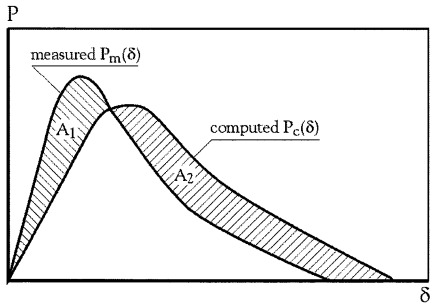

if $A_1 < A_2$ then $\Delta D_{fc} = 1 - A_1/A_2$

if $A_1 > A_2$ then $\Delta D_{fc} = 1 - A_2/A_1$

$\Delta D_{fc,max} = 0.1$

Figure 32: First accuracy check: comparison of toughness between computed and measured P-δ *curves*

The first criterion is not sufficient. Although the maximum deviation in toughness might be restricted to 10%, deviations in load might still exceed this 10%. Therefore, in a second check, the deviations between the measured load $P_m(\delta)$ and the computed load $P_c(\delta)$ are restricted to a maximum of 10% in the first part of the measured P-δ curve. As mentioned earlier, the first part of the P-δ curve is of most practical interest. In the scope of this research the deviations in load are checked up to a displacement δ^*_m, which corresponds to a 75% level of the peak load (see Figure 33).

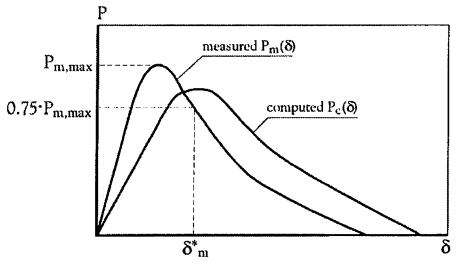

for $\delta \leq \delta^*_m$:

if $P_m(\delta) > P_c(\delta)$ then $1 - P_c(\delta)/P_m(\delta) < 0.1$

if $P_m(\delta) < P_c(\delta)$ then $1 - P_m(\delta)/P_c(\delta) < 0.1$

Figure 33: Second accuracy check: comparison of load level between computed and measured P-δ *curves*

3.2 *Computational versus mean test results*

Kooiman [Kooiman, 2000] showed the computational effect of each input parameter in the constitutive material relations on the load-crack opening curves. It was shown that the post-peak behaviour in the material relation for compression does not influence the load-bearing capacity in bending. However, the assumption for the post-peak behaviour in compression can affect the deformation capacity of a SFRC cross-section. It has been found that an idealised linear compressive softening branch up to a strain of 10‰ leads to good results.

The effect of the value of the linear elastic strain limit in tension on the P-δ curve is negligible. Only the pre-peak behaviour of SFRC is influenced by this assumption.

Furthermore, it was shown that mean P-δ curves from three-point bending tests can be easily described by means of a bilinear stress-crack width relation by using inverse analysis. After numerous inverse analyses it was found that in case of medium strength SFRC (mix composition 2 from Table 2) with 60 kg/m^3 of hooked-end steel wire fibres, the describing parameters of the stress-crack width relation can be determined as follows:

- The value of the mean uni-axial tensile strength of the composite material is determined from the mean value of the tensile splitting strength $f_{fctm,spl}$ derived from splitting tests on cubes. The ratio $f_{fctm,ax}/f_{fctm,spl}$ is in between 0.70 and 0.80.
- The equivalent post-cracking strength to tensile strength ratio $f_{fct,eq,bil}/f_{fctm,ax}$ is in between 0.20 and 0.30.
- The ratio w_c/w_0 is about 0.20.
- The critical crack width to fibre length ratio w_0/L_f is in the range of 0.33-0.425. In the next chapter, this will be further analysed. It will be shown that the critical crack width w_0 depends on the average fibre orientation, as a result of geometrical boundary conditions and the production process.

For the case of mix composition 2 with hooked-end steel wire fibres with an aspect ratio L_f/d_f of 60/0.75, Figure 34a shows the computed results. The load-displacement curves have been simulated for different beam widths and fit the mean experimental results with sufficient accuracy. Figure 34b shows that the simulated load-displacement curves of both the 300 mm and 450 mm wide beams fit the mean experimental results quite well. However, the simulated curve of the 150 mm wide specimens overestimates the mean results from 'standard' bending tests.

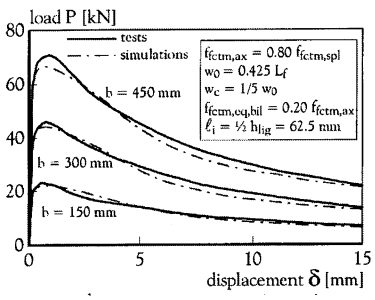

(a) 60 kg/m^3 60/0.75 hooked-end steel wire fibres

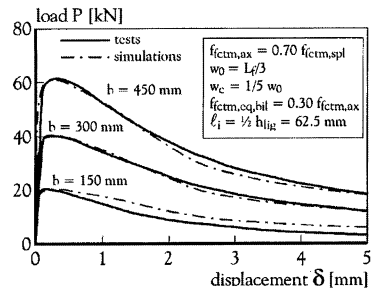

(b) 60 kg/m^3 30/0.5 hooked-end steel wire fibres

Figure 34: Simulated P-δ *curves of differently sized SFRC beams after adjustment of post-cracking behaviour*

4. Design relation for the post-cracking behaviour of SFRC

4.1 *Effect of the coefficient of variation on the characteristic strength values*

In the recommendations on test and design methods for SFRC of the RILEM Technical Committee 162-TDF [RILEM TC 162-TDF, 2000], the Student t-test was used to determine characteristic values for the post-cracking strengths. The RILEM Committee recommends the following equation to calculate the characteristic value $f_{fctk,eq}$ of the equivalent post-cracking strength in the stress-strain relation of Figure 1:

$$f_{fctk,\,eq} = f_{fctm,\,eq} - 1.645 \cdot s_f \tag{4}$$

In equation (4) the t-test is used to define the lower value of the 80% confidence interval as the mean equivalent tensile strength $f_{fctm,eq}$ of the population, calculated with the help of statistical parameters s_{fs} and $f_{fctms,eq}$ from the series, consisting of n test results:

$$f_{fctm,\,eq} = f_{fctms,\,eq} - \frac{s_{fs} \cdot t_{10,\,n-1}}{\sqrt{n}} \tag{5}$$

In the second term of equation (4), s_f is the standard deviation of the population. This standard deviation s_f is defined as the upper value of the 80% confidence interval:

$$s_f = s_{fs} \cdot \left(1 + \frac{s_{fs} \cdot t_{10,\,n-1}}{f_{fctm,\,eq} \cdot \sqrt{n}}\right) \tag{6}$$

Substituting equations (5) and (6) in equation (4), the latter becomes:

$$f_{fctmk,\,eq} = f_{fctms,\,eq} - \frac{s_{fs} \cdot t_{10,\,n-1}}{\sqrt{n}} - 1.645 \cdot s_{fs} \cdot \left(1 + \frac{s_{fs} \cdot t_{10,\,n-1}}{f_{fctm,\,eq} \cdot \sqrt{n}}\right) \tag{7}$$

To determine the effect of the coefficient of variation V_R on the characteristic value of the equivalent strength in the post-cracking behaviour, both arguments of equation (7) are divided by $f_{fctms,eq,bil}$.

$$\frac{f_{fctk,\,eq}}{f_{fctms,\,eq}} = 1 - \frac{V_R \cdot t_{10,\,n-1}}{\sqrt{n}} - 1.645 \cdot V_R \cdot \left(1 + \frac{s_{fs} \cdot t_{10,\,n-1}}{f_{fctm,\,eq} \cdot \sqrt{n}}\right) \tag{8}$$

The above mentioned approach is quite conservative. Not only the lower value of the 80% confidence level is used for the mean value of the population, but it is also assumed that the standard deviation of the population s_f is higher than the standard deviation of the test series. Based on equation (8), Figure 35a shows the effect of the coefficient of variation V_R on the characteristic value of the equivalent post-cracking strength $f_{fctk,eq}$. Obviously, this value decreases as the coefficient of variation increases. The number of tests determines the slope of the decreasing lines.

Figure 35b shows the effect of the coefficient of variation V_R on the characteristic value of the equivalent post-cracking strength $f_{fctk,eq,bil}$ according to the Bayesian technique. This approach is described in Eurocode 1 [ENV 1992-1-1, 1996] for situations, in which V_R is not known, but must be estimated from the sample. Compared to the frequency approach used in equation (8), the Bayesian technique is much simpler and less conservative. This approach will be used hereafter for the determination of characteristic values. The characteristic values according to this approach are determined with the help of the following equation:

$$\frac{f_{fctk,eq}}{f_{fctms,eq}} = 1 - V_R \cdot t_{10,n-1} \cdot \sqrt{1+\frac{1}{n}} \tag{9}$$

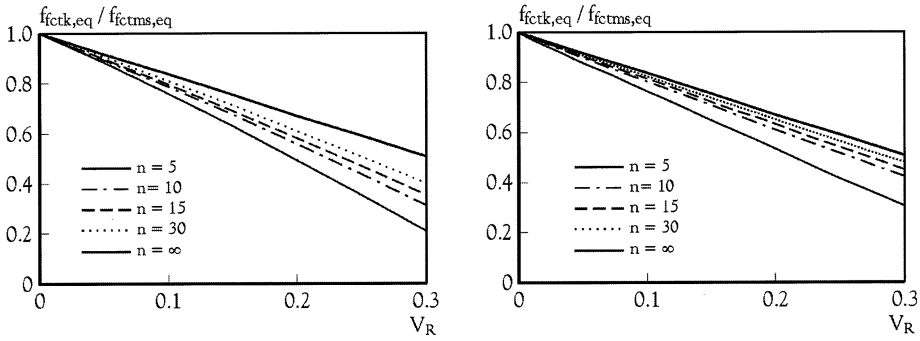

(a) $f_{fctk,eq}$ according to [RILEM TC 162-TDF, 2000] *(b) $f_{fctk,eq}$ according to Eurocode 1*

Figure 35: Effect of the coefficient of variation and the number of specimens on characteristic values

4.2 *Material safety factors for the post-cracking behaviour of SFRC*

According to Eurocode 1 [ENV 1992-1-1, 1994], the partial safety factor should be calculated as follows, in case of a normally distributed stochastic variable:

$$\gamma_R = (1 + |\alpha_R| \cdot \beta \cdot V_R) \tag{10}$$

For a lognormal distributions, Kooiman [Kooiman, 2000] used the following equation:

$$\gamma_R = \left((|\alpha_R| \cdot \beta - 1.645) \cdot V_R\right) \tag{11}$$

Eurocode 1 demands a reliability index b of 1.5 and 3.8 for the SLS and ULS respectively and uses values of 0.8 and 0.7 for a_R and a_Q respectively. The coefficient of variation in load V_Q depends on the loading condition under consideration and V_R on the uncertainty in resistance. According to

Nowak and Collins [Nowak & Collins, 2000], there are three possible sources of uncertainty in resistance in the case of concrete structures: uncertainty in material properties (M), uncertainty in geometrical properties (S) and inadequacy of the material model (A). The coefficient of variation in resistance V_R is the result of the following equation:

$$V_R = \sqrt{(V_M)^2 + (V_S)^2 + (V_A)^2} \tag{12}$$

4.3 *Bilinear design relationship for the post-cracking behaviour of SFRC*

Figure 36 shows the stress-crack width relation SFRC that can be used for design purposes. The describing parameters of this relation are the design values of the uni-axial tensile strength $f_{fctd,ax}$, the equivalent post-cracking strength $f_{fctd,eq,bil}$, the characteristic crack width w_c and critical crack width w_0.

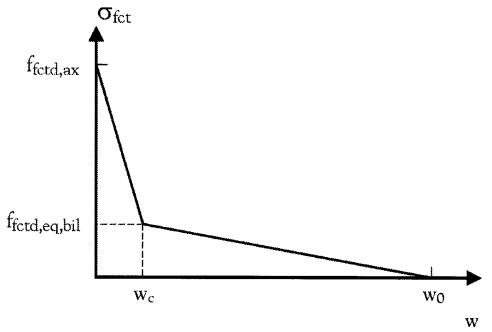

Figure 36: Bilinear post-cracking material relation for SFRC

Determination of the material safety factor for linear elastic behaviour of SFRC

The design value of the uni-axial tensile strength $f_{fctd,ax}$ for use in simulations of the flexural behaviour of cross-sections can be determined as follows:

$$f_{fctd,ax} = \frac{f_{fctk,ax}}{\gamma_{fct,el}} \tag{13}$$

The characteristic tensile strength $f_{fctk,ax}$ can be determined as follows:

$$f_{fctk,ax} = (1 - 1.645 \cdot V_R) \cdot f_{fctm,ax} \tag{14}$$

In Sections 4.1 and 4.2 it is shown how to calculate characteristic strength values and material safety factors. It is also shown that the characteristic strength and the material safety factor very much depend on the coefficient of variation in resistance V_R. By Equation (12) it is shown that the uncertainty in resistance not only depends on the scatter in material behaviour, expressed by the coefficient of variation in material properties (V_M), but also on uncertainty in geometrical properties (V_S) and the inadequacy of the method of analysis (V_A). As the fibre reinforcement considered in the scope of this research only starts acting after cracking of the matrix, it is reasonable to assume that V_M in the linear elastic behaviour of SFRC is equal to the value of V_M for plain concrete, which is 0.15. Accounting for a 10% uncertainty in dimensions and an accuracy of 10% of the material model, the coefficient of variation in resistance V_R becomes:

$$V_R = \sqrt{(0.15)^2 + (0.10)^2 + (0.10)^2} = 0.21$$

Following Eurocode 1, the material safety factor for plain concrete γ_{ct} is calculated according to equation (11):

$$\gamma_{ct} = 1 + \exp(-0.8 \cdot 3.8 \cdot 0.21) = 1.53$$

Initially, the mean uni-axial tensile strength $f_{fctm,ax}$ is determined from tensile splitting tests. As it was already shown, in the case of 60/0.75 fibres $f_{fctm,ax}$ is determined as follows:

$$f_{fctm,\,ax} = 0.8 \cdot f_{fctm,\,spl} \tag{15}$$

In the case of 30/0.75 fibres:

$$f_{fctm,\,ax} = 0.7 \cdot f_{fctm,\,spl} \tag{16}$$

Determination of the design value of the equivalent post-cracking strength $f_{fctd,eq,bil}$ of SFRC
The characteristic value of the equivalent post-cracking strength $f_{fctk,eq,bil}$ can be calculated with the following equation, which is based on equation (9):

$$\frac{f_{fctk,\,eq,\,bil}}{f_{fctm,\,eq,\,bil}} = 1 - V_R \cdot t_{10,\,n-1} \cdot \sqrt{1 + \frac{1}{n}} \tag{17}$$

The equivalent post-cracking strength can be expressed as the product of a large number of variables. It depends on the packing density, the water-binder ratio, the bond strength, the aspect ratio and the added fibre volume. It is therefore assumed that the distribution of this post-cracking

strength is lognormal. The material safety factor for the post-cracking behaviour is calculated with the help of equation (11). The design value is determined as follows:

$$f_{fctd,\,eq,\,bil} = \frac{f_{fctk,\,eq,\,bil}}{\gamma_{fct,\,spl}} \tag{18}$$

Section 3 showed that the inverse modelling procedure results in simulations that fit the mean test results quite well. The bilinear post-cracking relation used in the multi-layer procedure can easily result in a fit with an accuracy of 5%. The deviation in dimensions in practice is estimated to be 10%. Table 4 shows the effect of an increasing coefficient of variation V_R on the post-cracking material safety factor $\gamma_{fct,pl}$, based on equation (11). The influence factor α_R is again assumed to be equal to 0.8 and the reliability index β is 3.8.

Tabel 4. Post-cracking material safety factor $\gamma_{fct,pl}$ for SFRC

	$V_R = 0.05$	$V_R = 0.10$	$V_R = 0.15$	$V_R = 0.20$	$V_R = 0.25$	$V_R = 0.30$
$\gamma_{fct,pl}$	1.07	1.14	1.23	1.32	1.42	1.52

It is obvious that V_R strongly affects the design value. As Table 4 shows, the post-cracking material safety factor $\gamma_{fct,pl}$ increases from 1.07 to 1.52 when the coefficient of variation in resistance increases from 0.05 to 0.30, assuming that $\alpha_R = 0.8$ and $\beta = 3.8$.
As Section 2.4 showed, the coefficient of variation in material behaviour V_M (=V_G) can vary in between 0.05 and 0.28 in test specimens. It was shown that a large scatter occurs in 'standard' SFRC test specimens with a critical combination of concrete quality and fibre volume. It was also shown that this scatter strongly decreases in specimens with larger cross-sections. Based on this knowledge a material factor of 1.52 seems conservative. It is unclear, however, what is the magnitude of the variation in practice. As long as this variation in practice cannot be predicted with sufficient accuracy, it is recommended to use the conservative material factor of 1.52 for structural design purposes.

5. Concluding remarks and future perspectives

5.1 Conclusions

This paper provides a procedure to develop a reliable, bilinear stress-crack width relation to describe the post-cracking behaviour of SFRC. With the help of inverse analysis, the material model can be used to fit mean results from three-point bending tests on medium strength SFRC with sufficient accuracy (<5%). Furthermore, this paper provides relations to determine design values in the material model, based on common reliability methods. Taking variation in load and resistance into account, material safety factors were determined for the post-cracking behaviour of SFRC. The resulting design model can be easily used to perform structural design calculations, although these calculations are limited to cross-sectional analyses.

Three-point bending tests were carried out in order to investigate the scatter in the post-cracking behaviour of SFRC. The test results showed a wide range of scatter, as the coefficient of variation V_M varied between 0.05 and 0.28, depending on the specimen size, the number of fibres in the cross-section and the concrete strength.

The influence of scatter, expressed by the coefficient of variation V_M, on the design value of the equivalent post-cracking strength is considerable. Depending on the number of tests performed and the coefficient of variation, the design value of the equivalent post-cracking strength decreases considerably. It is not clear whether the observed scatter in test results applies for practical applications. Although the scatter seemed to decrease for increasing beam sizes, the scatter in practice also depends on the effectiveness of the fibre reinforcement. This depends on the fibre orientation as well as the orthogonal direction(s) of the occurring tensile stress(es).

5.2 *Future perspectives*

The application of SFRC in slabs, tunnel linings or underwater concrete can only be stimulated when it can be proven that the fibre reinforcement contributes to the resistance of the structure to the applied loads. The question, therefore, is no longer how to model the post-cracking behaviour of the material but in what way can the favourable post-cracking behaviour be taken into account in structural calculations? Important in that respect is that the redistributing capacity of the SFRC structure can be demonstrated by determining to what extent the external load can be increased before statically indeterminate structures fail.

Structural calculations using Finite Element Methods may be useful in providing insight into the real contribution of fibre reinforcement to the structural load-bearing capacity. In that respect, the smeared crack approach seems attractive to use. The only problem is that the stress-crack width relation needs to be transformed into a stress-strain relation using the average crack spacing. This is however hard to determine and does not only depend on the material properties. Whether or not multiple cracking occurs also depends on the structural system, the load configuration and the geometry of the structure. Therefore, the discrete crack approach seems more appropriate to use. By carrying out structural analyses with a varying number of discrete cracks on different locations, the insight into the structural behaviour of SFRC can be enhanced.

Acknowledgements

This paper reports on a research project carried out at the Stevin Laboratory of the Delft University of Technology. Support of technicians and staff of the Concrete Structures Group is highly appreciated. The financial support of the Civil Engineering Department of the Directorate-General of Public Works and Water Management, the Dutch Centre for Underground Construction (COB) and the Dutch Foundation for Technical Sciences (STW) is also gratefully acknowledged.

References

ACI Committee 544, *Design considerations for Steel Fibre Reinforced Concrete,* ACI Structural Journal, Vol. 85 (6), 1988, pp. 563-580.

BAZANT, Z.P., *Size effect in blunt fracture: concrete, rock, metal,* ASCE Journal of Engineering Mechanics 110, 1984, pp. 518-535.

ENV 1992-1-1, *Eurocode 1: Basis of design and actions on structures – Part 1: Basis of design*, CEN, 1994.

FALKNER, H. & V. Henke, *Steel Fibre Reinforced Concrete for underwater concrete slabs*, Proceedings of the International RILEM Conference 'Production Methods & Workability of Concrete', Paisley, Scotland, June 3-5, 1996, pp. 79-92

GUINEA, G.V., Planas, J. & M. Elices, *Measurement of the fracture energy using three point bend tests: Part 1 - Influence of experimental procedures*, Materials & Structures, Vol. 25 (148), 1992, p. 212-218.

HORDIJK, D., *Local approach to fatigue of concrete,* PhD-thesis, Department of Concrete Structures, Faculty of Civil Engineering, Delft University of Technology, the Netherlands, 1991, pp. 131-134.

KOOIMAN, A.G., *Staalvezelbeton in de Tweede Heinenoord Tunnel, het definitieve ontwerp*, Design calculations of SFRC segments for application in the Second Heinenoord tunnel (in Dutch), Stevinreport no. 25.5.97-3, Delft University of Technology, Netherlands, 1997, p. 25.

KOOIMAN, A.G., Van der Veen, C. & M.H. Djorai, *Steel Fibre Reinforced Concrete segments in the Second Heinenoord Tunnel,* Proceedings of the fib Symposium 1999 'The bridge between people', Prague, Czech Republic, 12-15 October 1999, pp. 685-690.

KOOIMAN, A.G., *Modelling Steel Fibre Reinforced Concrete for Structural Design*, PhD-thesis, Delft University of Technology, October 2000, p. 184.

KÖRMELING, H.A., *Strain rate and temperature behaviour of steel fibre concrete in tension*, PhD-thesis, Department of Concrete Structures, Faculty of Civil Engineering, Delft University of Technology, the Netherlands, 1986, pp. 4.13-4.14.

NAAMAN, A.E., *Fibres with hardening bond,* Proceedings of the IIIrd International RILEM Workshop 'High Performance Fibre Reinforced Cementitious Composites' (HPFRCC 3), Mainz, 1999, pp. 471-486.

NOWAK, A.S. & K.R. Collins, *Reliability of Structures*, McGraw-Hill Book Company, 2000, pp. 181-208.

PEDERSON, C, *New production processes, Materials and Calculation* Techniques for Fibre Reinforced Pipes, PhD-thesis, Department of Structural Engineering and Materials, Technical University of Denmark, 1996.

RILEM TC 162-TDF Draft Recommendation, *Test and design methods for SFRC, bending test,* Materials and Structures Vol. 33, 2000, pp. 3-5.

RILEM TC 162-TDF Draft Recommendation, *Test and design methods for SFRC*, σ-e design method, Materials and Structures, Vol. 33, 2000, pp. 75-81.

RILEM TC-89 FMT Draft Recommendation, *Determination of the fracture parameters of plain concrete using three-point bend tests*, Materials & Structures, Vol. 23, 1990, pp. 457-460.

ROELFSTRA, P.E. & F.H. WITTMANN, *Numerical method to link strain softening with failure of concrete,* In 'Fracture Toughness and Fracture Energy', Edited by F.H. Witmann, Elsevier, London, 1986.

SCHNÜTGEN, *Structural applications of steel fibre reinforced concrete,* accepted for publication in the proceedings of the RILEM workshop 'Structural applications of SFRC', in Milan, Italy, April 2000.

SCHNÜTGEN, *Design of steel fiber reinforced concrete in precast structures*, Proceedings of the International workshop on structural applications of steel fibre reinforced concrete, Milan, Italy, April 2000.

STROBAND, J., *Standardisation of test methods for Steel Fibre Reinforced Concrete,* Laboratory report (in Dutch) no. 25.5.98-14, Delft University of Technology, Netherlands, 1998, p. 41.

WITTMANN, F.H., ROKUGO, K., BRÜHWILER, E., MIHASHI, H. & SIMONIN, P., *Fracture energy and strain softening of concrete as determined by means of compact tension specimens,* Materials and Structures, Vol. 20, 1988, pp. 21-32.

Notations and Symbols

α_R	= influence factor to emphasise scatter in resistance	[-]
β	= reliability index	[-]
δ	= crack opening displacement	[mm]
δ_c	= maximum displacement in compressive zone	[mm]
δ_i	= displacement in layer i	[mm]
δ_{notch}	= displacement at notch tip	[mm]
δ_s	= crack opening displacement at test stop[	mm]
δ'	= crack opening displacement after weight compensation	[mm]
ΔD_{fc}	= deviation in toughness between measured and computed load-displacement curves	[kNmm]
$\Delta D_{fc,w}$	= contribution to toughness by dead weight of the beam	[kNmm]
ε_{cc}	= compressive strain in plain concrete	[‰]
ε_{ct}	= linear elastic strain limit of plain concrete in tension	[‰]
$\varepsilon_{ct,ax}$	= strain limit at uni-axial tensile strength	[‰]
ε_{fcc}	= compressive strain in fibre reinforced cementitious composite	[‰]
ε_{fct}	= tensile strain in fibre reinforced cementitious composite	[‰]
σ_{cc}	= compressive stress in plain concrete	[N/mm^2]
σ_{ct}	= tensile stress in plain concrete	[N/mm^2]
σ_{fcc}	= compressive stress in fibre reinforced cementitious composite	[N/mm^2]
σ_{fct}	= tensile stress in fibre reinforced cementitious composite	[N/mm^2]
σ_i	= stress in ith layer in multi-layer procedure	[N/mm^2]
γ_{cc}	= material safety factor for plain concrete in compression	[-]
γ_{ct}	= material safety factor for plain concrete in tension	[-]
$\gamma_{fct,pl}$	= material safety factor for the post-cracking behaviour of SFRC	[-]
γ_R	= material safety factor	[-]
a	= notch depth of specimen	[mm]
A_c	= surface of the cross Section	[mm^2]
b	= width of specimen	[mm]
d_f	= fibre diameter	[mm]
D_{fc}	= toughness of SFRC	[kNmm]
f_{ccm}	= mean compressive strength of plain concrete matrix	[N/mm^2]
$f_{ctm,ax}$	= tensile strength of plain concrete matrix	[N/mm^2]
f_{fcd}	= design compressive strength of SFRC	[N/mm^2]
f_{fck}	= characteristic compressive strength of SFRC	[N/mm^2]
f_{fcm}	= mean compressive strength of SFRC	[N/mm^2]
$f_{fctd,ax}$	= design value of the uni-axial tensile strength of SFRC	[N/mm^2]
$f_{fctd,eq,bil}$	= design value of equivalent post-cracking strength in bilinear softening relationship	[N/mm^2]
$f_{fctk,ax}$	= characteristic axial tensile strength of SFRC	[N/mm^2]
$f_{fctk,eq}$	= characteristic value of equivalent post-cracking strength of SFRC	[N/mm^2]
$f_{fctk,eq,bil}$	= characteristic value of equivalent post-cracking strength in bilinear softening relationship	[N/mm^2]
$f_{fctm,ax}$	= mean axial tensile strength of SFRC	[N/mm^2]
$f_{fctm,eq}$	= mean value of equivalent post-cracking strength of SFRC	[N/mm^2]
$f_{fctm,eq,bil}$	= mean value of equivalent post-cracking strength of SFRC in bilinear softening relationship	[N/mm^2]

$f_{fctm,spl}$	= mean tensile splitting strength of SFRC	[N/mm^2]
$f_{fctms,eq}$	= mean equivalent post-cracking strength of SFRC determined from test sample	[N/mm^2]
$f_{fctms,eq,bil}$	= mean equivalent post-cracking strength of SFRC in bilinear relationship	
G_{fc}	= energy absorption capacity of SFRC	[kN/mm]
G^i_{fc}	= energy absorption capacity of the ith SFRC specimen in the test series	[kN/mm]
G_{fcm}	= mean energy absorption capacity of SFRC	[kN/mm]
$G_{fcm,2.0}$	= mean energy absorption capacity at a crack opening displacement of 2.0 mm	[kN/mm]
h	= depth of specimen	[mm]
h_i	= layer depth	[mm]
h_{lig}	= effective beam depth = h-a	[mm]
l	= span length of specimen	[mm]
l_i	= influence length	[mm]
L_f	= fibre length	[mm]
LVDT	= Linear Variable Displacement Transducer	
M_{int}	= internal bending moment	[kN]
n	= number of specimens in a test series	[-]
n_{fm}	= mean number of fibres in cross Section	[-]
n_l	= number layers in multi-layer procedure	[-]
N	= normal force	[kN]
P	= applied load on specimen	[kN]
P_c	= computed load on specimen	[kN]
P_m	= measured load on specimen	[kN]
$P_{m,max}$	= measured peak load on specimen	[kN]
P′	= applied load on specimen after weight compensation	[kN]
s_f	= standard deviation of population of f_{fc}	[N/mm^2]
s_{fs}	= standard deviation of f_{fc} in test sample[	N/mm^2]
s_G	= standard deviation of population of G_{frc}	[kN/mm]
$t_{\alpha/2,n-1}$	= value for a t-test with (1-α)_100% confidence level	[-]
V_A	= coefficient of variation in uncertainty in material or structural	[-]
V_f	= volume fraction of fibres	[%]
V_G	= coefficient of variation in energy absorption capacity	[-]
V_M	= coefficient of variation in material properties	[-]
V_R	= coefficient of variation in resistance	[-]
V_S	= coefficient of variation in geometrical properties	[-]
w	= crack width	[mm]
w_0	= critical crack width	[mm]
w_c	= characteristic crack width	[mm]
z_i	= distance of ith layer in multi-layer procedure	[mm]